JACS
JOURNAL OF THE AMERICAN CHEMICAL SOCIETY

Article

pubs.acs.org/JACS

Kinetic and Mechanistic Assessment of Alkanol/Alkanal Decarbonylation and Deoxygenation Pathways on Metal Catalysts

Elif I. Gürbüz,[†,‡] David D. Hibbitts,[†] and Enrique Iglesia*[,†,‡]

[†]Department of Chemical and Biomolecular Engineering and [‡]Division of Chemical Sciences, E. O. Lawrence Berkeley National Laboratory, University of California at Berkeley, Berkeley, California 94720, United States

Supporting Information

ABSTRACT: This study combines theory and experiment to determine the kinetically relevant steps and site requirements for deoxygenation of alkanols and alkanals. These reactants deoxygenate predominantly via decarbonylation (C−C cleavage) instead of C−O hydrogenolysis on Ir, Pt, and Ru, leading to strong inhibition effects by chemisorbed CO (CO*). C−C cleavage occurs via unsaturated species formed in sequential quasi-equilibrated dehydrogenation steps, which replace C−H with C−metal bonds, resulting in strong inhibition by H_2, also observed in alkane hydrogenolysis. C−C cleavage occurs in oxygenates only at locations vicinal to the C═O group in RCCO* intermediates, because such adjacency weakens C−C bonds, which also leads to much lower activation enthalpies for oxygenates than hydrocarbons. C−O hydrogenolysis rates are independent of H_2 pressure and limited by H*-assisted C−O cleavage in RCHOH* intermediates on surfaces with significant coverages of CO* formed in decarbonylation events. The ratio of C−O hydrogenolysis to decarbonylation rates increased almost 100-fold as the Ir cluster size increased from 0.7 to 7 nm; these trends reflect C−O hydrogenolysis reactions favored on terrace sites, while C−C hydrogenolysis prefers sites with lower coordination, because of the relative size of their transition states and the crowded nature of CO*-covered surfaces. C−O hydrogenolysis becomes the preferred deoxygenation route on Cu-based catalysts, thus avoiding CO inhibition effects. The relative rates of C−O and C−C cleavage on these metals depend on their relative ability to bind C atoms, because C−C cleavage transitions states require an additional M−C attachment.

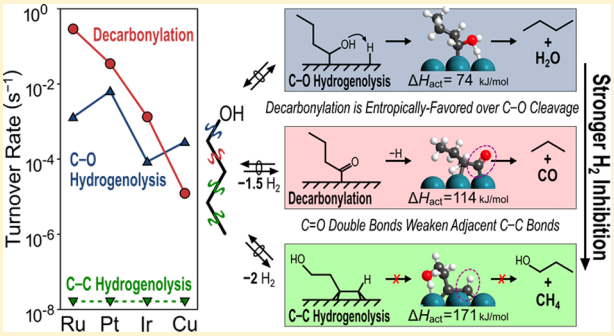

1. INTRODUCTION

Oxygen must be removed from biomass-derived molecules to render them useful as fuels and chemicals, but such processes remain challenging because of their significant energy and H_2 requirements.[1,2] Oxygen removal strategies include C−O hydrogenolysis, using H_2 to remove oxygen as H_2O (hydrodeoxygenation), and C−C hydrogenolysis reactions that form a shorter carbon backbone and CO (decarbonylation) or CO_2 (decarboxylation) as coproducts. Alkanols and alkanals are ubiquitous in biomass-derived streams, and a more detailed understanding of the relevant mechanisms by which these molecules react on metal surfaces is essential to choose catalytic systems for their efficient conversion in reforming,[3] direct fuel cells,[4] and oxidation reactions.[5]

The conversion of many complex alkanol substrates[1,6−8] has been studied on several metal catalysts in the aqueous phase, but without detailed mechanistic conclusions, at least in part, because of the mass transfer limitations and nonideal thermodynamics, ubiquitous in such aqueous media. Rates of ethanol and 1-propanol decarbonylation reactions were 10−100 times larger than C−O hydrogenolysis rates on single crystals of Pt,[13] Pd,[9−11] and Ni.[12] Density functional theory (DFT) treatments of the conversion pathways for ethanol,[14−17] ethylene glycol,[18] and glycerol[19] on Group VIII metals (Pt, Pd, Ir, Ru, Rh) indicate that H-removal steps occur before C−C or C−O cleavage, similar to the extensive dehydrogenation that precedes C−C cleavage of alkanes.[20,21] High-resolution electron energy loss spectra,[9] the identity and desorption dynamics of the products formed from preadsorbed ethanol,[10−12] and DFT calculations[14−17] on single crystals, however, have not led to a consensus about the structure and the degree of unsaturation of the relevant intermediates and transition states. Also, while C−O hydrogenolysis of biomass-derived furanic species was reported on Cu in gaseous[22,23] and aqueous[24,25] media, its turnover rate and the C−C and C−O bond cleavage selectivities have not been systematically compared among Cu and Group VIII metals. These unresolved or unaddressed matters have prevented precise assessments of the origins of reactivity in C−C and C−O cleavage of alkanols/alkanals and of how C−C cleavage differs in mechanistic detail among alkanols, alkanals, and alkanes.

Here, we report turnover rates and their dependence on reactant and product concentrations for reactions of 1-butanol/H_2 mixtures on supported Ir, Pt, Ru, and Cu clusters at conditions relevant to their practical use. Decarbonylation

Received: May 23, 2015
Published: September 10, 2015

DOI: 10.1021/jacs.5b05361
J. Am. Chem. Soc. 2015, 137, 11984−11995

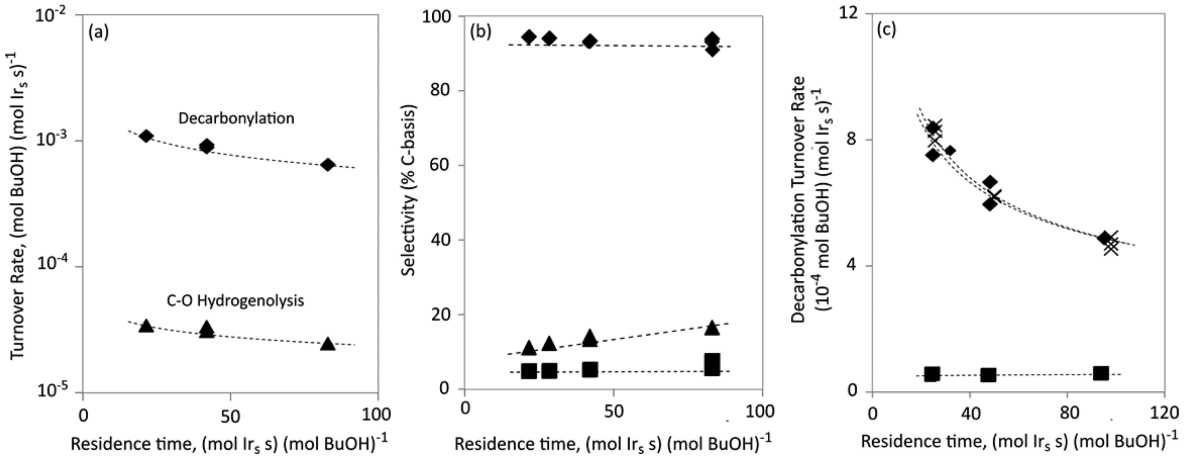

Figure 1. Effects of residence time on (a) decarbonylation (◆) and C−O hydrogenolysis (▲) turnover rates, (b) propane (◆), CH_4 (▲, ×4), and butane (■) carbon (propane and C1 molecules (CO, CH_4) formed in equimolar amounts at all conditions), and (c) decarbonylation turnover rates with no H_2O or CO added (◆), 1 kPa H_2O added (X) and 1 kPa CO added (■) (1 wt % Ir/SiO_2 (0.7 nm), 523 K, 2 MPa H_2, 5 kPa 1-butanol). 1-Butanol/butanal pool conversions range from 1.2% to 6.4% at these residence times. Dashed lines represent trendlines.

occurs with much higher turnover rates than C−O hydrogenolysis on small clusters of Ir, Pt, and Ru (∼1 nm mean diameter), and no other C−C cleavage reactions occur. DFT-derived activation barriers indicate that the presence of C−O double bonds (in alkanol/alkanal-derived intermediates) significantly weakens adjacent C−C bonds, resulting in lower barriers for C−C cleavage vicinal to −CO groups (decarbonylation) than for C−C cleavage at other backbone positions. H_2 pressure inhibits decarbonylation and has no effect on C−O hydrogenolysis, and these H_2 effects are consistent with kinetically relevant transition states of decarbonylation that are more dehydrogenated than those for C−O hydrogenolysis, confirmed here using DFT methods. The ratio of C−O hydrogenolysis to decarbonylation for 1-butanol is much lower than unity on small (∼1 nm) Ir, Ru, and Pt catalysts and approaches unity only on larger (7 nm Ir) clusters, indicating that C−O hydrogenolysis occurs on low-index terrace sites that become more prevalent on larger clusters, while decarbonylation is much less sensitive to surface coordination. C−O hydrogenolysis is the predominant route on Cu because CO* and C* form weaker bonds on Cu than Group VIII metals, consistent with much lower decarbonylation turnover rates on Cu (10−100 times smaller) than on Ir, Pt, and Ru catalysts.

2. EXPERIMENTAL METHODS

2.1. Synthesis and Characterization of SiO_2-Supported Ir, Pt, Ru, and Cu Clusters. SiO_2 (Davisil 646, 300 m^2 g^{-1}) was treated in flowing dry air (Praxair, 99.99%, 5.0 cm^3 g^{-1} s^{-1}) by heating to 823 K (at 0.03 K s^{-1}) and holding for 5 h. Ir (1.0% wt), Ru (0.5% wt) and Cu (5% wt) precursors were deposited onto the treated silica using incipient wetness impregnation with aqueous solutions of Ir (H_2IrCl_6, Strem Chemicals, 99%), Ru (Ru(NO) $(NO_3)_3$, Alfa-Aesar, 32% wt Ru), and Cu ($Cu(NO_3)_2{\cdot}2.5H_2O$, Strem Chemicals, 99.5%), which were mixed with triethanolamine (TEA, Sigma-Aldrich, 97%) (20:1 mol) solutions in deionized (DI) water (17.9 MΩ resistivity) before impregnation; these procedures have been reported to lead to small clusters of uniform size for Ru-based catalysts and were adapted here for the synthesis of Ir and Cu.[21,26] Ir−SiO_2 samples with different Ir contents (2.0% and 3.0% wt) were prepared by varying the concentration of TEA and H_2IrCl_6 in the impregnating solution while maintaining a 20:1 molar ratio. Pt/SiO_2 (1.0% wt) was prepared by strong electrostatic adsorption of $Pt(NH_3)_4(NO_3)_2$ (Sigma-Aldrich, 99.9%) onto SiO_2 (Davisil 646) using a NH_4OH solution.[27]

All samples were dried in flowing dry air (Praxair, 99.99%, 5.0 cm^3 g^{-1} s^{-1}), then treated under flowing dry air and 50% H_2/He (Praxair, 99.999%, 1.0 cm^3 g^{-1} s^{-1}) to reduce the metals and obtain various cluster sizes. The details of the drying, treatment, and reduction conditions for each catalyst (Ir (1.0% wt), Ir (2.0% wt), Ir (3.0% wt), Ru (0.5% wt), Pt (1.0% wt), and Cu (5.0% wt)) may be found in the Supporting Information (SI). All samples were cooled to ambient temperature and passivated in flowing 0.5% O_2/He (Praxair, 99.99%, 1.0 cm^3 g^{-1} s^{-1}) for 3 h before exposure to ambient air.

The number of exposed Ir, Pt and Ru atoms in each catalyst was determined from volumetric uptakes of H_2 at 298 K using previously reported procedures[21] and assuming adsorption stoichiometries of 1/1 for H/M_s.[28] The mean cluster diameter for each sample was estimated from the measured dispersion by assuming hemispherical crystallites and the atomic density of the bulk metals.[29,30] Cluster sizes for Ir (1.0% wt, 140% dispersion), Ir (2.0% wt, 26% dispersion), Ir (3.0% wt, 13% dispersion), Ru (0.5% wt, 98% dispersion), and Pt (1.0% wt, 155% dispersion) were determined to be 0.7, 3.6, 7.0, 0.6, and 0.7 nm, respectively. These cluster sizes were confirmed with transmission electron microscopy (TEM) in previous work.[20,21] For Cu, the cluster size distribution was determined to be 5.1 nm by TEM imaging corresponding to a fractional dispersion of 0.20 for the case of hemispherical clusters with the density of bulk Cu metal.[30] The details of the TEM measurements and dispersion calculations can be found in the SI.

2.2. Catalytic Reactions of 1-Butanol. 1-Butanol (Sigma-Aldrich, 98%) conversion rates and selectivities were measured in a stainless steel tubular flow reactor (3/8″ O.D.) with plug-flow hydrodynamics at 483−523 K, 1−5 kPa 1-butanol, and 1−3 MPa H_2. The details of the temperature, pressure, gas, and liquid flow controls can be found in the SI. Catalysts were mixed with SiO_2 (Cab-O-Sil HS-5, washed with deionized water and treated in flowing dry air at 793 K for 5 h). Decarbonylation and C−O hydrogenolysis turnover rates (Figure 1) were unaffected by dilution (SiO_2/Ir-SiO_2 = 0−4), indicating that neither bed temperature gradients nor contributions from the support influenced measured turnover rates. All samples were treated in flowing H_2 (Praxair, 99.999%; 50 cm^3 g^{-1} s^{-1}) at ambient pressure by heating to 673 K at 0.083 K s^{-1} and holding for 2 h before rate measurements.

Reactant and product concentrations were measured by gas chromatography (Agilent GC, 5890) using a methyl silicone capillary column (HP-1, Agilent, 50 m × 0.32 mm × 1.05 μm) with a flame ionization detector and a packed column (Porapak Q, Alltech, 80/100, 12′ × 1/8′) with a thermal conductivity detector. All rates are reported at differential conversions (<5%) in reference to the alkanal/alkanol reactant pool to avoid axial concentration gradients. Turnover rates are normalized by the number of surface metal atoms determined by H_2

DOI: 10.1021/jacs.5b05361
J. Am. Chem. Soc. 2015, 137, 11984−11995

Scheme 1. Reaction Pathways Involved in 1-Butanol Conversion[a]

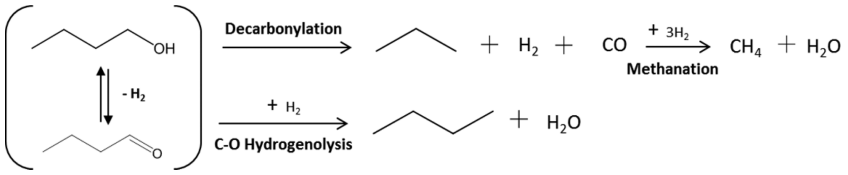

[a]Stoichiometries are based on the use of 1-butanol (instead of its equilibrated butanal dehydrogenation product) as the reactant.

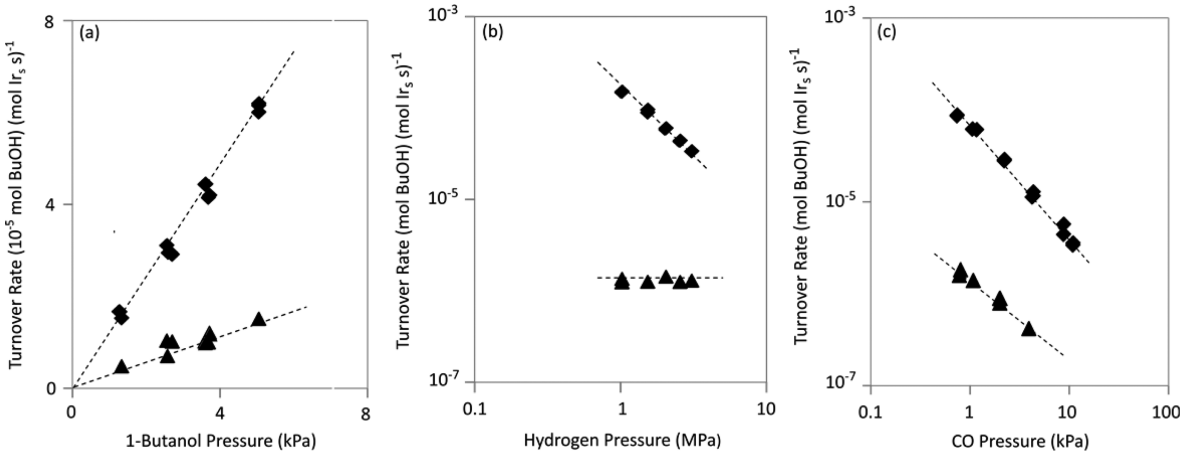

Figure 2. Decarbonylation (◆) and C−O hydrogenolysis (▲) turnover rates on 1 wt % Ir/SiO_2 (0.7 nm) at 523 K. (a) 1-Butanol pressure effects at 2 MPa H_2 and 1 kPa CO. (b) H_2 pressure effects at 5 kPa 1-butanol and 1 kPa CO. (c) CO pressure effects at 5 kPa 1-butanol and 2 MPa H_2. Dashed lines are representative of turnover rates calculated using the regressed kinetic and thermodynamic parameters and the proposed rate eqs (eqs 2 and 6 for decarbonylation and C−O hydrogenolysis, respectively).

chemisorption for Ir, Pt, and Ru and by TEM for Cu. Selectivities are reported as the percentage of the C atoms in the 1-butanol/butanal equilibrated pool converted that appears within a given product.

2.3. Computational Methods. Periodic DFT calculations were performed using the Vienna ab initio simulation package (VASP)[31−34] with planewaves constructed using projector augmented-wave (PAW) potentials.[35,36] Exchange and correlation energies were determined using revised Perdew−Burke−Ernzerhof (RPBE) form of the generalized gradient approximation (GGA).[37−39] Transition-state structures were obtained for each elementary reaction using the nudged elastic band (NEB) method[40,41] and the dimer method.[42] The details of these electronic structure calculations may be found in the SI.

3. RESULTS AND DISCUSSION

3.1. 1-Butanol Turnover Rates and Selectivity on Ir/SiO_2. 1-Butanol can react reversibly on Ir/SiO_2 to form butanal and H_2 (dehydrogenation) with an approach to equilibrium (η):

$$C_4H_9OH \overset{K_{deh}}{\longleftrightarrow} C_4H_8O + H_2, \quad \eta = \frac{P_{H_2}P_{butanal}}{P_{butanol}}\frac{1}{K_{deh}} \qquad (1)$$

value of 0.7−1 even at the low 1-butanol conversions in this study (0.8% to 6.4%), allowing butanol and butanal to be treated as a lumped reactant pool in all reported turnover rates and selectivities. 1-Butanol can also form (i) propane and CO (decarbonylation; C−C hydrogenolysis), (ii) butane and H_2O (C−O hydrogenolysis), and (iii) CH_4 and H_2O (methanation) via a secondary reaction of CO and H_2 (Scheme 1).

1-Butanol decarbonylation rates were >10 times higher than C−O hydrogenolysis rates (Ir/SiO_2; Figure 1a, 0.7 nm clusters; 473−523 K, 1−3 MPa H_2), as also reported for ethanol[9−14,17,43] and propanol[13] on Pt, Pd, Ru, and Ni catalysts at lower H_2 pressures (<0.1 MPa, 400−523 K). Propanol, ethanol, and ethane were not detected as products, indicating that only C−C bonds vicinal to the O atom are cleaved, consistent with 1-propanol reactions on Pd[11] and Pt.[13] CO_2 was also not detected, indicating CO did not react with H_2O formed in situ. 1-Butanol decarbonylation and C−O hydrogenolysis turnover rates were unaffected by the presence of additional SiO_2 present as physical mixture (SiO_2/Ir-SiO_2 = 0−4, Cab-O-Sil HS-5, washed with deionized water and treated in flowing dry air at 793 K for 5 h), indicative of monofunctional reactions. Propane and butane selectivities depended weakly on residence time and reactant pool conversion (Figure 1b), even though they form directly from equilibrated butanol-butanal mixtures, because their formation rates are inhibited to different extents by the CO formed in decarbonylation reactions. CH_4 selectivity was low and increased with residence time (Figure 1b), together with a decrease in CO selectivity, because of methanation reactions. Propane and C_1 molecules (CO, CH_4) formed in equimolar amounts at all conditions.

Decarbonylation and C−O hydrogenolysis turnover rates decreased with increasing residence time (Ir/SiO_2, Figure 1a), even at very low reactant pool conversions (2−6%), indicating that products (CO and/or H_2O) inhibit these reactions. Rates were unaffected by added H_2O (Figure 1c) at pressures (1 kPa H_2O) above those prevalent during 1-butanol reactions (<0.003 kPa H_2O); therefore, H_2O-derived intermediates do not account for the observed product inhibition. CO added to 1-butanol/H_2 reactants (1 kPa vs <0.07 kPa during reaction; Figure 1c) led to more than a 10-fold decrease in rates; rates were no longer influenced by conversion when CO was present. Turnover rates were stable with time on stream (Figure S1), indicating that CO* did not irreversibly poison the Ir metal, but

DOI: 10.1021/jacs.5b05361
J. Am. Chem. Soc. 2015, 137, 11984−11995

instead inhibited rates through quasi-equilibrated adsorption/desorption events. These data show that CO strongly inhibits rates by competitive adsorption, leading to kinetically detectable CO* coverages, even at very low conversions (2–6%) and CO pressures (0.04–0.07 kPa). Such CO inhibition effects are also evident in aqueous and gas-phase reforming of oxygenates (ethylene glycol, glycerol, sorbitol)[18,44] on Pt and Ni surfaces and in ethanol decarbonylation on Pt surfaces;[16] these strong inhibitory effects of CO* remain influential even at the higher and more relevant H_2 pressures (1–3 MPa) and low conversions of the present study.

3.2. Effects of 1-Butanol, H_2, and CO Pressures on Decarbonylation Turnover Rates. Decarbonylation turnover rates were proportional to 1-butanol pressure (Figure 2a) and inversely dependent on H_2 (Figure 2b) and CO (Figure 2c) pressures on Ir/SiO_2. The observed decrease in decarbonylation rates with increasing H_2 pressure is consistent with the involvement of unsaturated species, formed via quasi-equilibrated dehydrogenation steps, as intermediates in the formation of the transition states that mediate kinetically relevant steps.

Scheme 2 depicts a sequence of elementary steps that accounts for the observed kinetic effects of alkanol, CO, and H_2 pressures on 1-butanol decarbonylation rates (Figure 2) and which is consistent with DFT calculations described below. Steps 2.1 and 2.2 in Scheme 2 involve quasi-equilibrated H_2 dissociation and molecular adsorption of 1-butanol, respectively. Adsorbed butanol undergoes quasi-equilibrated O–H and C–H activation events (2.3 to 2.5) to form acyl intermediates ($C_2H_5CH_2C^*O$, the * appears to the right of an atom bound to a surface atom) and an irreversible C–H activation at the α-C atom to form $C_2H_5CH^*C^*O$ species (2.6). The $C_2H_5CH^*C^*O$ species undergo another C–H activation to form $C_2H_5C^*C^*O$ (2.7), which cleaves its C–C bond to form $C_3H_5^*$ and CO* (2.8).

These elementary steps and reversibility assumptions (Scheme 2) lead to the rate equation:

$$\frac{r}{[L]} = \frac{\alpha(\mathrm{BuOH})}{(H_2)^{1.5}(1 + K_{CO}(CO))^2} \quad (2)$$

Scheme 2. Proposed Intermediates and Sequence of Elementary Steps Involved in Decarbonylation of 1-Butanol on Ir Clusters[a]

(2.1)	$H_2 + 2^* \rightleftharpoons 2\,H^*$	K_H
(2.2)	$C_2H_5CH_2CH_2OH + ^* \rightleftharpoons C_2H_5CH_2CH_2OH^*$	K_{BUOH}
(2.3)	$C_2H_5CH_2CH_2OH^* + ^* \rightleftharpoons C_2H_5CH_2CH_2O^* + H^*$	$K_{OH,1}$
(2.4)	$C_2H_5CH_2CH_2O^* + ^* \rightleftharpoons C_2H_5CH_2CHO^* + H^*$	$K_{CH,1}$
(2.5)	$C_2H_5CH_2CHO^* + ^* \rightleftharpoons C_2H_5CH_2CO^* + H^*$	$K_{CH,2}$
(2.6)	$C_2H_5CH_2CO^* + ^* \rightarrow C_2H_5CHCO^* + H^*$	$k_{CH,3}$
(2.7)	$C_2H_5CHCO^* + ^* \rightarrow C_2H_5CCO^* + H^*$	$k_{CH,x}$
(2.8)	$C_2H_5CCO^* + ^* \rightarrow C_3H_5^* + CO^*$	$k_{C\text{-}C}$
(2.9)	$C_3H_5^* + 3H^* \rightleftharpoons C_3H_8 + 4^*$	K_{C3H8}
(2.10)	$CO + ^* \rightleftharpoons CO^*$	K_{CO}

[a]The * denotes an unoccupied surface site; k_x and K_x are kinetic constants for forward steps and equilibrium constants, respectively. Quasi-equilibrated steps are noted by a circle over the double arrows.

where the denominator terms account for the relative coverages of vacant sites (*) and (CO*) species and K_{CO} is the equilibrium constant for CO* adsorption. The α term in eq 2 represents an effective rate constant for decarbonylation:

$$\alpha = K_{BuOH}K_{OH,1}K_{CH,1}K_{CH,2}K_{H_2}^{-1.5}k_{CH,3} \quad (3)$$

with the rate and equilibrium constants defined for the elementary steps in Scheme 2. The α term reflects the contributions of C–H activation in $C_2H_5CH_2C^*O$ species (Scheme 2, step 2.6) as the sole kinetically relevant step. The values of α (2.9 ± 0.13 kPa$^{0.5}$ s^{-1}) and K_{CO} ($6.3 \times 10^{-1} \pm 2.4 \times 10^{-2}$ kPa^{-1}) were obtained by regressing all rate data (Figure 3, 523 K, 0.7 nm Ir) to the functional form of eq 2. Fractional CO* coverages derived from this K_{CO} value range from 0.30 to 0.85 as CO pressures increased from 0.8 to 8 kPa at 523 K. Alternate decarbonylation pathways, such as those involving kinetically relevant C–C activation in $C_2H_5CH_2CO^*$ (instead of C–H activation in $C_2H_5CH_2C^*O$) would have led to rates also given by eq 2, but are ruled out here because of their significantly larger DFT-derived barriers compared with the steps in Scheme 2 (discussed in detail below). Eq 2 assumes that H* species are minority surface species, even at 1–3 MPa H_2 pressures (Figure 3). This conclusion is consistent with the insensitivity of C–O hydrogenolysis rates to H_2 pressure and with the similar effects of H_2 pressure on Ir particles with different mean diameters (0.7–7 nm), which suggest that H* coverages are not kinetically detectable at these conditions (1–5 kPa 1-butanol, 1–3 MPa H_2, 0.8–8 kPa CO at 523 K), as further discussed in the SI (Figures S2 and S3).

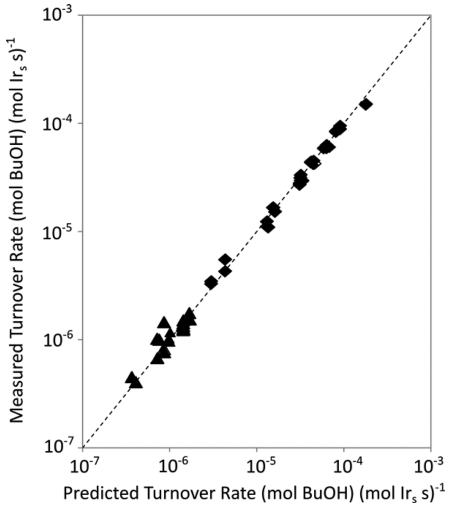

Figure 3. Measured decarbonylation (◆) and C–O hydrogenolysis (▲) turnover rates on 1% wt Ir/SiO_2 and those predicted from regression of the rate data to the functional forms of eqs 2 (◆) and 6 (▲), respectively, at 523 K.

Previous rate data and theoretical assessments for alkane hydrogenolysis[20,21] have indicated that one or more C atoms undergo C–H activation to form C–M bonds before C–C cleavage. The requirement for bound C atoms and the equilibrated nature of alkanol-alkanal interconversions (Section 3.1) suggest the involvement of RCH*O, RC*O, and RC*OH species (where R = CH_3CH_2, CH_3CH^*, and CH_3C^*) in decarbonylation (C–C cleavage). DFT calculations were carried out for these species instead of 1-butanol/butanal to decrease conformational diversity and computational intensity

DOI: 10.1021/jacs.5b05361
J. Am. Chem. Soc. 2015, 137, 11984–11995

Scheme 3. DFT-Calculated Effective Enthalpy Barriers ($\Delta H^{\ddagger}$, black, bold font), Intrinsic Activation Enthalpies (ΔH_{act}, blue, left of slash), and Reaction Enthalpies (ΔH_{rxn}, red, right of slash) for Propanol Decarbonylation Pathways[a]

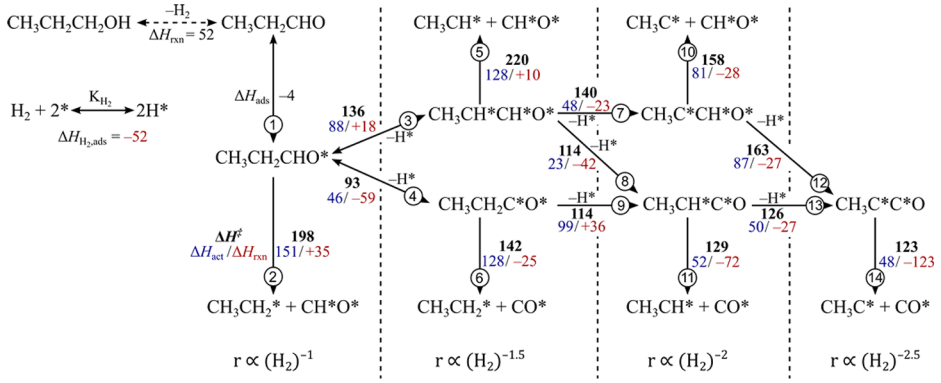

[a]Reversible steps are represented by double arrows (↔) and irreversible steps are represented by single arrows (→). Reaction numbers used throughout the text are given within circles (①, e.g.) on top of each reaction arrow. Structures for reactant, transition, and product states for all reactions shown in this scheme are available in the SI (Figures S4–S15).

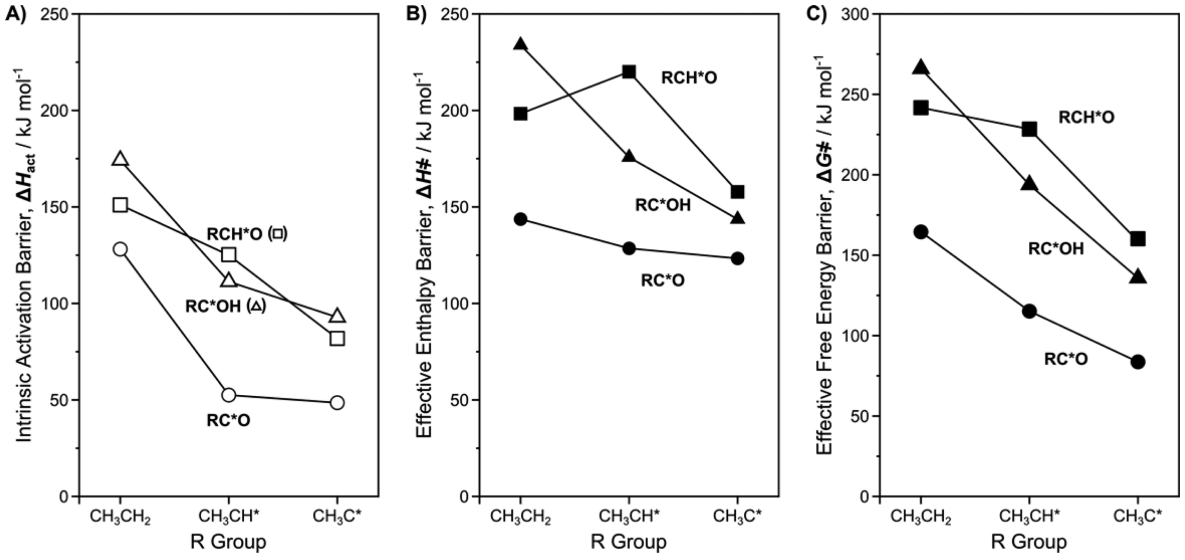

Figure 4. (A) ΔH_{act} (open symbols, difference between transition states and relevant precursors); (B) $\Delta H^{\ddagger}$ (closed symbols, difference between transition states and gas-phase propanol); and (C) $\Delta G^{\ddagger}$ (at 483 K, 1 bar) and for C–C activations of RCH*O (■), RC*OH (▲), and RC*O (●) intermediates where R = CH_3CH_2, CH_3CH^*, and CH_3C^*.

and because C–C hydrogenolysis occurs exclusively at the C–C bond vicinal to the –OH group (Section 3.1).

Adsorbed propanal can react with a vacant site and undergo C–C cleavage to form vicinal $CH_3CH_2^*$ and CH*O* species (Scheme 3, Step 2); ΔH_{act} values (151 kJ mol^{-1}) for this step are much larger than C–H bond activation at the α-C position in adsorbed propanal to form an $CH_3CH^*CH^*O$ and H* (Step 3, $\Delta H_{act,3}$ = 88 kJ mol^{-1}). Subsequent C–H activation at the α-C position would then form $CH_3C^*CH^*O$ (Step 7, $\Delta H_{act,7}$ = 48 kJ mol^{-1}), thus C–H activations at the α-C are more facile than direct C–C activation of propanol. Intrinsic (ΔH_{act}, enthalpy differences between transition states and the corresponding precursors) and effective ($\Delta H^{\ddagger}$, difference between the transition state and propanol in the gas-phase) enthalpy barriers for C–C cleavage reactions both decrease as more H atoms are removed from the α-C atom (Figures 4 and 5) for all RCH*O species (R = CH_3CH_2, CH_3CH^*, CH_3C^*).

Propanal can also undergo C–H activation at the carbonyl C atom in RCH*O to form RC*O species ($CH_3CH_2C^*O$, $CH_3CH^*C^*O$, and $CH_3C^*C^*O$). C–C cleavage in RC*O occurs with smaller ΔH_{act} and $\Delta H^{\ddagger}$ than for C–C cleavage in RCH*O (Figures 4 and 5). ΔH_{act} and $\Delta H^{\ddagger}$ values decreased as H atoms are removed from the α-C atom in both RCH*O and RC*O species, because H-removal occurs with the concomitant formation of C–M bonds (Figure 5), which weakens C–C bonds, as also shown for C–C cleavage steps alkane hydrogenolysis.[20,21,45,47–49]

Successive C–H activation events in propanol-derived species can form RC*OH species (R = CH_3CH_2, CH_3CH^*, CH_3C^*), which can undergo C–C cleavage (Scheme S1, SI). C–C cleavage in RC*OH (R = CH_3CH_2, CH_3CH^*, CH_3C^*) occurs with higher ΔH_{act} and $\Delta H^{\ddagger}$ than in RC*O (Figures 4 and 5). ΔH_{act} and $\Delta H^{\ddagger}$ values for C–C cleavage in RC*OH both decreased as α-C atoms lose H atoms, as also found for RC*O and RCH*O species (Figure 4). Transition states for C–C cleavage in RC*OH exhibit much longer C–O bonds than in RC*O (Figure 5), and the bonding geometry at the C atom for RC*OH and RC*O species indicates a shift from sp^3 to sp^2 hybridization (from RC*OH to RC*O). These changes in local geometry indicate that C═O bonds are present in

DOI: 10.1021/jacs.5b05361
J. Am. Chem. Soc. 2015, 137, 11984–11995

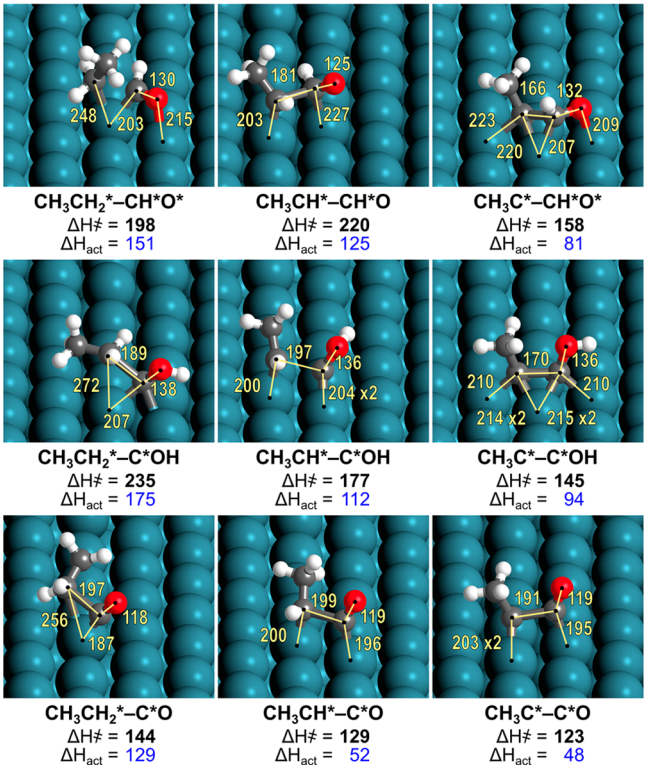

Figure 5. Transition-state structures, $\Delta H^{\ddagger}$ (black, boldface), and ΔH_{act} (blue) for C–C activations or RCH*O*, RCOH* and RCO* intermediates. Bond distances (in pm) are shown in yellow; "x2" indicates a C–M bond with a similar (±1 pm) bond length which cannot be seen at the viewing angle used.

RC*O but not in RC*OH; these C═O bonds weaken adjacent C–C bonds, thus favoring C–C bond cleavage in RC*O over similar reactions in RC*OH.

C–C cleavage in $CH_3C^*C^*O$ (Step 14) shows the lowest ΔH_{act} (48 kJ mol^{-1}) and $\Delta H^{\ddagger}$ (123 kJ mol^{-1}) values among all nine C–C cleavage steps considered (Steps 2, 5, 6, 12, and 14 in Scheme 3, and Steps 27, 30, and 33 in Scheme S1). The relative rates of C–C cleavage in these nine intermediates (RCH*O, RCOH*, and RCO* with R = CH_3CH_2, CH_3CH^*, and CH_3C^*) were evaluated by determining the maximum possible rate of each C–C cleavage step. This maximum rate requires that all previous steps be quasi-equilibrated, thus resulting in a thermodynamically limited pool of reactant precursors. Transition-state theory formalisms then give these maximum rates for each C–C cleavage steps as

$$\frac{r_{max}}{[L]} = \frac{k_B T}{h} e^{(-\Delta G^{\ddagger}/RT)} \frac{(\text{alkanol})}{(H_2)^{y/2}} \frac{1}{[1 + K_{CO}(CO)]^2} \quad (4)$$

where k_B and h are the Boltzmann and Planck constants, respectively, and y represents the number of H atoms removed before C–C cleavage. Since rates depend on Gibbs free energies ($\Delta G^{\ddagger}$), entropy ($\Delta S^{\ddagger}$) was accounted for by calculating the relative magnitudes of the C–C cleavage in the nine intermediates in Figures 4 and 5. $\Delta S^{\ddagger}$ values increase with increasing extent of dehydrogenation because H_2 (g) is evolved upon forming each transition state. C–C cleavage in $CH_3C^*C^*O$ (with the lowest $\Delta H^{\ddagger}$, Figure 4B) shows the largest $\Delta S^{\ddagger}$ values and the smallest $\Delta G^{\ddagger}$ (Figure 4C), indicating that C–C cleavage occurs almost exclusively via $CH_3C^*C^*O$ intermediates.

In alkane hydrogenolysis on metals, C–C cleavage steps are irreversible and kinetically relevant, while C–H activation steps are quasi-equilibrated.[20,21] If this were the case for alkanol/alkanal decarbonylation reactions, C–C cleavage via $CH_3C^*C^*O$ species would be given by

$$\frac{r}{[L]} = \frac{\alpha(\text{BuOH})}{(H_2)^{2.5}(1 + K_{CO}(CO))^2} \quad (5)$$

inconsistent with measured rates ($r \sim (H_2)^{-1.5}$; eq 2). These DFT treatments, taken together with measured rates, indicate that while C–C cleavage may indeed occur preferentially in $CH_3C^*C^*O$ species during decarbonylation, some preceding C–H activation steps may not achieve equilibrium. The measured H_2 effects on decarbonylation rates implicate the activation of a C–H bond in $CH_3CH_2C^*O^*$ species (Step 9) as the kinetically relevant decarbonylation step. These inferences are made rigorous by the seamless coupling of theory and experiment in this study; mechanistic conclusions would have been inaccurate if based on kinetic analysis or theoretical treatments alone. Next, we assess the differences in C–C activation events among alkanols/alkanals and alkanes.

3.3. Effects of Proximity to Carbon–Oxygen Bond on the Cleavage Rates of C–C Bonds. C–C bonds in alkanols cleave after four H atoms are removed from the C atoms involved in the cleaved C–C bond based on experimental and DFT results shown in Section 3.2, as for C–C hydrogenolysis of ^{1}C–^{1}C, ^{1}C–^{2}C, and ^{2}C–^{2}C bonds (^{1}C and ^{2}C represent primary and secondary carbons, respectively, with C–C activation as the kinetically relevant step) in acyclic and cyclic alkanes.[20,21,45,50] In contrast with alkanes, C–C hydrogenolysis in alkanols involves: (i) O–H activation to form C═O bonds that weaken vicinal C–C bonds; (ii) C–H activation, instead of C–C activation, as kinetically relevant step; and (iii) the

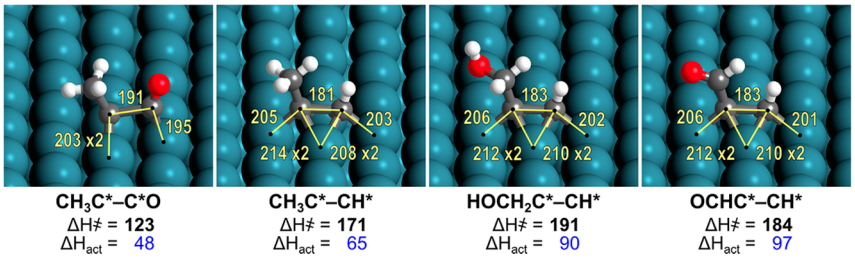

Figure 6. Transition-state structures, $\Delta H^{\ddagger}$, and ΔH_{act} for C–C cleavage via decarbonylation ($CH_3C^*–CO^{*\ddagger}$) and via RC*–CH*‡ transition states (R = $-CH_3$, $-CH_2OH$, $-CHO$). Important bond distances (in pm) are shown in yellow; "x2" indicates that a bond which cannot be seen at the viewing angle used has a similar bond length.

DOI: 10.1021/jacs.5b05361
J. Am. Chem. Soc. 2015, 137, 11984–11995

selective activation of C−C bonds adjacent to C=O groups. The weakening of C−C bonds by the vicinal C=O moieties is evident from the DFT-calculated ΔH_{act} values for C−C cleavage in $CH_3C^*C^*O$ (48 kJ mol^{-1}) and $CH_3C^*C^*H$ (65 kJ mol^{-1}). These ΔH_{act} values lead to much smaller $\Delta H^{\ddagger}$ values for decarbonylation (123 kJ mol^{-1}) than for alkane hydrogenolysis (170 kJ mol^{-1}), consistent with 1-butanol/butanal decarbonylation turnover rates that are >10^4 times larger than for C−C hydrogenolysis in *n*-butane on Ir (0.7 nm) at similar conditions (523 K, 2 MPa H_2).[21]

Here, we also examine the C−C cleavage of alkanols at bonds without neighboring O atoms. Intrinsic activation enthalpies (ΔH_{act}) are much higher for C−C cleavage in $CH^*C^*CH_2OH$ (90 kJ mol^{-1}) and in CH^*C^*CHO (97 kJ mol^{-1}) than for the respective propane-derived intermediates (65 kJ mol^{-1} for $CH^*C^*CH_3$) (Figure 6). Decarbonylation has the lowest $\Delta H^{\ddagger}$ among these C−C bond activations (Figure 6), consistent with the exclusive formation of C_3 and C_1 molecules from 1-butanol reactants (Section 3.1).

3.4. Effects of 1-Butanol, H_2, and CO Pressures on C−O Hydrogenolysis Turnover Rates. Measured C−O hydrogenolysis rates are proportional to 1-butanol pressure (Figure 2a) and inversely dependent on CO pressure (Figure 2c) on Ir/SiO_2, as also observed for decarbonylation rates (Figure 2a,c). C−O hydrogenolysis rates do not depend on H_2 pressure, while decarbonylation reactions are inhibited by H_2 (cf. Figure 2b). These data indicate that kinetically relevant C−O hydrogenolysis transition states contain the same number of H atoms as 1-butanol, making them much less dehydrogenated than the transition states for decarbonylation, as also proposed based on theoretical treatments of ethanol reactions on Pt(111).[17]

Scheme 4 depicts a plausible sequence of elementary steps for C−O hydrogenolysis of 1-butanol; these steps are

Scheme 4. Proposed Sequence of Steps and Intermediates in C−O Hydrogenolysis of 1-Butanol on Ir Clusters[a]

(4.1) $H_2 + 2^* \rightleftharpoons 2\,H^*$ K_H

(4.2) $C_2H_5CH_2CH_2OH + ^* \rightleftharpoons C_2H_5CH_2CH_2OH^*$ K_{BUOH}

(4.3) $C_2H_5CH_2CH_2OH^* + ^* \rightleftharpoons C_2H_5CH_2CHOH^* + H^*$ K_{CH}

(4.4) $C_2H_5CH_2CHOH^* + H^* \rightarrow C_2H_5CH_2CH^* + H_2O^*$ k_{C-O}

(4.5) $C_4H_8^* + 2H^* \rightleftharpoons C_4H_{10} + 3^*$ K_{C4H10}

(4.6) $H_2O + ^* \rightleftharpoons H_2O^*$ K_{H2O}

[a]The * denotes an unoccupied surface site; k_x and K_x are kinetic constants for forward steps and equilibrium constants, respectively.

consistent with the observed effects of alkanol and H_2 pressures on rates (Figure 2) and with theoretical estimates described below. Molecularly adsorbed butanol undergoes quasi-equilibrated C−H activation (4.3) to form $CH_3CH_2CH^*OH$, which then reacts in an irreversible step with H* with concerted O−H formation and C−O cleavage to form vicinal H_2O^* and $CH_3CH_2CH^*$ (4.4). The corresponding rate equation is

$$\frac{r}{[L]} = \frac{\beta(\mathrm{BuOH})}{(1 + K_{CO}(\mathrm{CO}))^2} \quad (6)$$

with β given by

$$\beta = K_{BuOH} K_{CH} k_{C-O} \quad (7)$$

with parameters defined in Scheme 4. Regressing all rate data to the functional form of eq 6 shows that the elementary steps in Scheme 4 accurately describes the measured C−O cleavage rates at all 1-butanol, H_2 and CO pressures (Figure 3). The parameter β in eq 7 is 6.0 ± 0.59 ×10^{-7} kPa^{-1} s^{-1} at 523 K; the K_{CO} value was slightly smaller for C−O hydrogenolysis (0.47 ± 0.06 kPa^{-1}) than for decarbonylation (0.63 ± 0.02 kPa^{-1}). The variance in K_{CO} values and the relationship between the types of sites involved in each reaction are discussed in Section 3.5.

Scheme 5 shows possible pathways and the corresponding enthalpic barriers for C−O hydrogenolysis of 1-propanol.

Scheme 5. DFT-Derived Effective Enthalpy Barriers ($\Delta H^{\ddagger}$, black, bold font), Intrinsic Activation Enthalpies (ΔH_{act}, blue, italic font), and Reaction Enthalpies (ΔH_{rxn}, red) for Propanol C−O Hydrogenolysis Pathways[a]

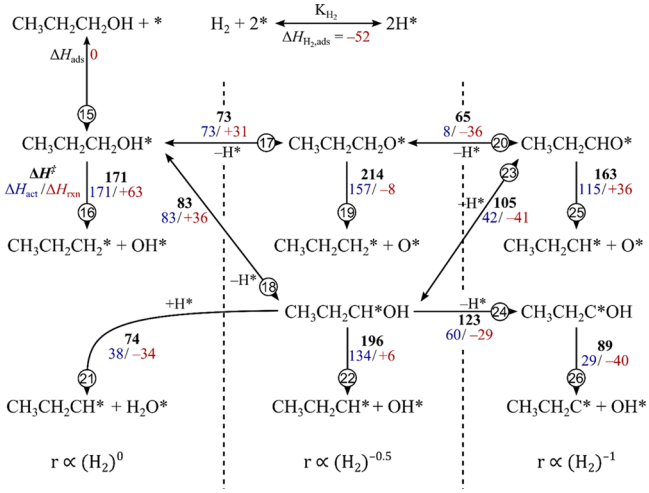

[a]Rate dependences on H_2 are based on the alkanol reactant. Reversible steps are represented by double arrows (↔), and irreversible steps are represented by single arrows (→). Reaction numbers used throughout the text are encircled (①, e.g.) above each reaction arrow. Structures for reactant, transition, and product states for all reactions shown in this scheme are available in the SI (Figures S4−S15). Color version available online.

Molecularly adsorbed propanol can react directly with a vicinal vacant site by cleaving its C−O bond and forming $CH_3CH_2CH_2$* and OH* (Step 16). This direct activation would lead to rates with the functional form of eq 6, but with a different chemical meaning of β. The intrinsic activation barrier for this step ($\Delta H_{act,16}$ = 171 kJ mol^{-1}) is much larger than for cleaving the O−H bond in 1-butanol to form propoxyl ($CH_3CH_2CH_2O^*$) and H* (Step 17, $\Delta H_{act,17}$ = 73 kJ mol^{-1}) or for cleaving the C−H bond in 1-butanol at the O-bound C atom to give hydroxypropyl species ($CH_3CH_2CH^*OH$) and H* (Step 18, $\Delta H_{act,18}$ = 83 kJ mol^{-1}). Thus, C−H and O−H activation steps occur before the C−O bond cleaves on Ir surfaces.

The reaction network in Scheme 5 includes six different C−O activation steps (Steps 16, 19, 21, 22, 25, and 26). Out of the six C−O activation routes, there are two pathways (Steps 16 and 21) involving transition states that contain eight H atoms and would lead to rates that are unaffected by H_2 pressure, as observed experimentally (Figure 2). C−O cleavage is mediated in molecularly adsorbed propanol (via reaction with a vicinal *) in Step 16 in the first route and in $CH_3CH_2CH^*OH$ species

DOI: 10.1021/jacs.5b05361
J. Am. Chem. Soc. 2015, 137, 11984−11995

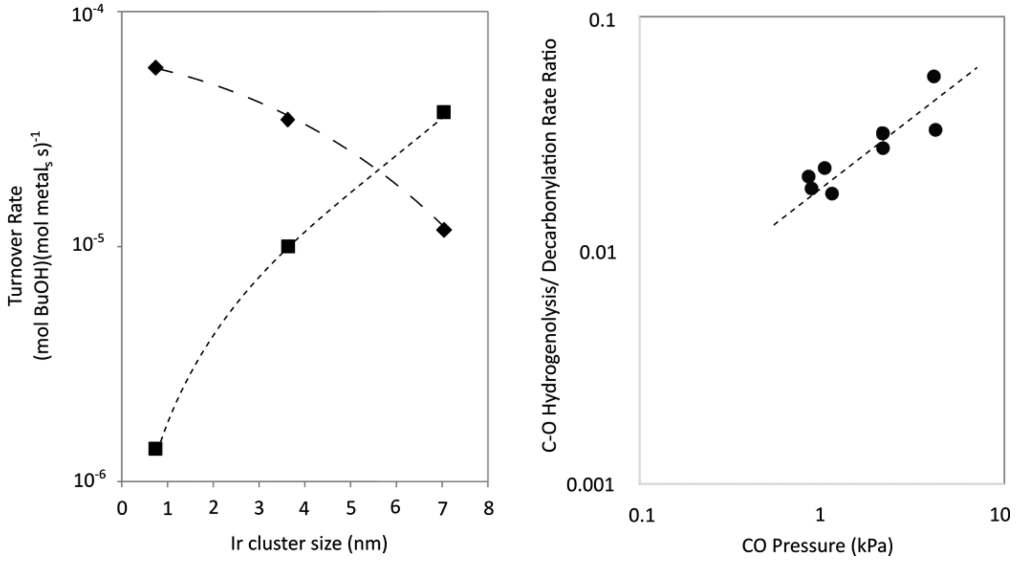

Figure 7. (a) Effect of Ir cluster size on decarbonylation (◆) and C−O hydrogenolysis (■) turnover rates (523 K, 5 kPa 1-butanol, 2 MPa H_2, 1 kPa CO). (b) Effect of CO pressure on the ratio of C−O to decarbonylation (523 K, 5 kPa 1-butanol, 2 MPa H_2). Dashed lines represent trends.

(via reaction with an additional H*) in Step 21 in the second route. The $\Delta H^{\ddagger}$ value for H*-assisted $CH_3CH_2CH^*OH$ activation ($\Delta H^{\ddagger}_{21}$ = 74 kJ mol^{-1}) is much smaller, however, than for direct C−O activation in molecularly adsorbed propanol (Step 16, $\Delta H^{\ddagger}$ = 171 kJ mol^{-1}), leading to a very small contribution from Step 16, as can be determined from the rate ratio of these two steps:

$$\frac{r_{16}}{r_{21}} = \frac{A_{16}}{A_{21}} e^{(\Delta H^{\ddagger}_{21} - \Delta H^{\ddagger}_{16})/RT} \quad (8)$$

with an exponential term much smaller than unity (2.1×10^{-10} at 523 K). These results indicate that C−O hydrogenolysis of alkanol-alkanal reactants proceeds predominantly via H*-assisted C−O activation in $CH_3CH_2CH^*OH$ species. The C−O bond in propanol weakens upon formation of a C−M bond during C−H activation to form $CH_3CH_2CH^*OH$; a vicinal H* then interacts with the lone pair in the O atom to assist the cleavage of the C−O bond. This mechanism is consistent with the independence of C−O hydrogenolysis rates on H_2 pressure (Figure 2).

The other four C−O activation routes in Scheme 5 (via Steps 19, 22, 24, or 25) involve kinetically relevant transition states with fewer H atoms than alkanol reactants and would thus lead to C−O hydrogenolysis rates that would decrease as H_2 pressure increases, in contrast with experiments (Figure 2b). Nevertheless, we consider such steps in detail in the SI (Section S7) for completeness and to confirm that these theoretical treatments can indeed rule out such sequences of elementary steps based on their activation free energies, in addition to comparisons with experiments. DFT-predicted effective free energy barriers confirm that H*-assisted activation of $CH_3CH_2CH^*OH$ is preferred over all other C−O activation routes. H*-assisted C−O activation proceeds with lower intrinsic enthalpy barriers than unassisted C−O activation in ring opening hydrogenolysis of heterocyclic oxygenates,[51] but was not considered for C−O activation in alkanol reactants in previous work, which only considered "unassisted" C−O cleavage reactions.[14,17]

3.5. Effects of Ir Cluster Size on Decarbonylation and C−O Hydrogenolysis Turnover Rates. C−O hydrogenolysis turnover rates increased by a factor of 30 with increasing cluster size (0.7−7 nm), while C−C hydrogenolysis turnover rates decreased about 5-fold (Figure 7a) at conditions (1 kPa CO) that lead to significant CO* coverages (based on regressed K_{CO} values in Sections 3.2 and 3.4), which implicates the preferential involvement of exposed atoms of different coordination in these two reactions. C−O hydrogenolysis occurs preferentially on exposed atoms with high coordination that prevail on low-index planes and larger clusters,[52] while lower-coordination atoms appear to favor C−C hydrogenolysis, despite C−C hydrogenolysis rates of alkanes occurring preferentially on higher-coordinated atoms.[50] The ratio of C−O to C−C hydrogenolysis rates increases with increasing CO pressure (Figure 7b; 0.7 nm Ir clusters), suggesting that C−O hydrogenolysis occurs on atoms that bind CO* more weakly than atoms involved in C−C hydrogenolysis, consistent with CO* binding energies that are weaker on low-index metal planes than on corner and edge atoms.[53]

These effects of Ir cluster size on decarbonylation and C−O hydrogenolysis turnover rates reflect the effects of surface coordination on the lumped rate constants α (eq 2) and β (eq 6) for decarbonylation and C−O hydrogenolysis, respectively, and the CO adsorption constants (K_{CO}). The lumped rate constants depend upon the free energies of surface-bound transition states ($G^{\ddagger}_{CH,3}$ for decarbonylation or $G^{\ddagger}_{C-O}$ for C−O hydrogenolysis) and gas-phase species (see Section S8 (SI) for more details). Bond-order conservation considerations would suggest that low-coordination atoms bind all adsorbed species (including transition states) more strongly;[54] thus, C−O and C−C hydrogenolysis rates would be higher on smaller clusters, but only at conditions of low CO* coverages, for which α and β solely determine turnover rates, but not for the turnover rates reported in Figure 7a measured at conditions (1 kPa CO) that lead to significant CO* coverages.

At high CO* coverages, it is the relative effects of coordination on α or β, and on K_{CO} (and thus on $G^{\ddagger}_{CH,3}$ or $G^{\ddagger}_{C-O}$, and G_{CO^*}) that determine their preference for atoms with a given coordination (see Section S8 (SI) for more details). Higher decarbonylation turnover rates on smaller particles indicate that low coordination atoms favor the binding

DOI: 10.1021/jacs.5b05361
J. Am. Chem. Soc. 2015, 137, 11984−11995

of its kinetically relevant transition state over the two CO* species that must be removed to bind it, while the opposite is the case for C−O hydrogenolysis reactions on Ir clusters. These considerations are illustrated by a reaction coordinate in Figure S16 and can be related to the differences in the binding strength of the two transition states. The kinetically relevant transition state for decarbonylation has two C−M bonds (of 204 and 232 pm) and one H−M bond (163 pm) (Figure 8a),

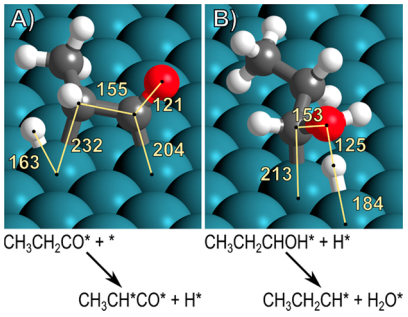

Figure 8. Structures for the kinetically relevant transition states for (A) decarbonylation (Step 2.6 of Scheme 2) and (B) C−O hydrogenolysis (Step 4.4 of Scheme 4). Notable bond distances shown in pm.

whereas the transition state for C−O hydrogenolysis contains just one C−M bond (213 pm) and one H−M bond (183 pm) (Figure 8b). The number and lengths of the bonds each kinetically relevant transition state forms to the surface indicate that the decarbonylation transition state is more strongly bound to the surface than the transition state for C−O hydrogenolysis, which proceeds via activation of the C−O bond by vicinal H* instead of metal-atom insertion into a C−H bond, as in decarbonylation.

The K_{CO} values regressed from eqs 2 and 6 for decarbonylation (0.63 ± 0.02 kPa^{-1}) and C−O hydrogenolysis (0.47 ± 0.06 kPa^{-1}) suggest that coverages are 0.3−0.4 ML at 1 kPa CO and 523 K on Ir clusters (0.7 nm), indicating that the observed size effects reflect the stabilization of transition states and CO* on crowded surfaces. In fact, CO* coverages are likely to be even higher because the Langmuir−Hinshelwood formalism used to derive eqs 2 and 6 assume that rate and equilibrium constants (α and K_{CO} in eq 2) remain unchanged as CO* coverages increase. Yet, CO* species impose repulsive forces on vicinal CO* or transition states, rendering such species less stable, as confirmed by theoretical treatments.[53,55] Such CO* coverage effects would cause the α and K_{CO} parameters in the rate equation (eq 2) to become smaller as CO* coverages increase with increasing CO pressure and thus invalidate the assumptions underlying the derivation of these Langmuir−Hinshelwood rate equations. If increasing CO* coverages decrease $\Delta G_{ads,CO}$ values (and thus K_{CO}) more than they decrease $\Delta G_{eff,C-C}$ (and thus α, eq 3), K_{CO} would be underestimated by eqs 2 and 6, indicating that actual CO* coverages are closer to 1 ML than those reported above (0.4 ML). Thus, the expectation for high CO* coverages suggests that the kinetically relevant transition state for decarbonylation has a smaller "footprint" on the catalyst surface than a pair of coadsorbed CO* species, partially due to the intact C−C bond of the transition state (whereas a pair of coadsorbed CO* species are not covalently bound to one another). These speculations also reveal the difficulties of applying Langmuir−Hinshelwood based rate equations to systems with strong co-adsorbate interactions that may confound kinetic analyses and lead to inconsistencies between coverages determined by kinetics, spectroscopy data, and theory.

3.6. Comparisons of 1-Butanol Turnover Rates and Selectivities on Pt, Ru, Ir, and Cu. Decarbonylation consumes less H_2 stoichiometrically than C−O hydrogenolysis, making the former a seemingly attractive deoxygenation route. Decarbonylation, however, forms CO molecules that strongly inhibit both deoxygenation routes. We consider in this section C−O hydrogenolysis selectivities on Ru, Pt, and Cu metal surfaces. Decarbonylation rates were 10−100 times higher than C−O hydrogenolysis rates on Ru/SiO_2 (0.6 nm), Pt/SiO_2 (0.7 nm), and Ir/SiO2 (0.7 nm) (Figure 9b), indicating that decarbonylation is the main decomposition pathway on Group VIII metals.[15,17] CO strongly inhibited decarbonylation and C−O hydrogenolysis rates on Pt and Ru (Figure 9a) as on Ir,

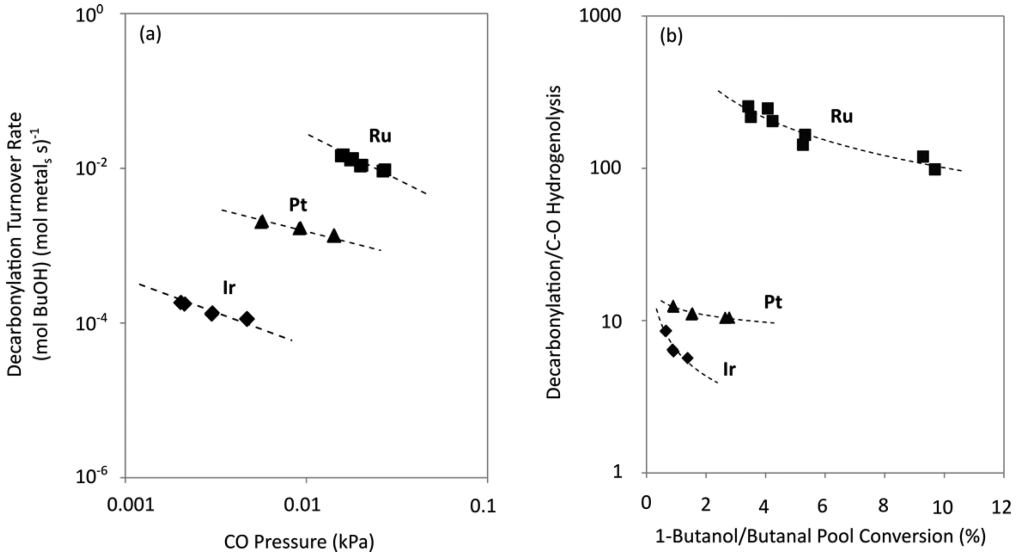

Figure 9. (a) Effect of CO (generated from 1-butanol/butanal conversion) pressure on decarbonylation turnover rates. (b) Effect of 1-butanol/butanal pool conversion on decarbonylation/C−O hydrogenolysis rate ratio on 1 wt % Ir/SiO_2 (0.7 nm, ◆), 1 wt % Pt/SiO_2 (0.7 nm, ▲), and 0.5 wt % Ru/SiO_2 (0.6 nm, ■) (483 K, 2 MPa H_2, 5 kPa 1-butanol). Dashed lines represent trends.

DOI: 10.1021/jacs.5b05361
J. Am. Chem. Soc. 2015, 137, 11984−11995

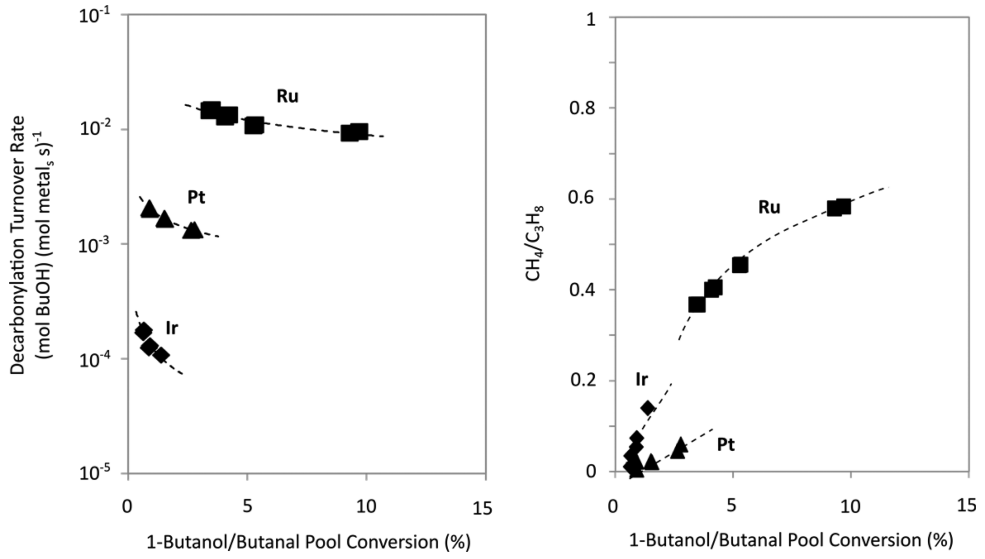

Figure 10. Decarbonylation turnover rate (a) and methane/propane ratio (b) with changing 1-butanol/butanal pool conversion on 1 wt % Ir/SiO_2 (0.7 nm, ◆), 1 wt % Pt/SiO_2 (0.7 nm, ▲), and 0.5 wt % Ru/SiO_2 (0.6 nm, ■) (483 K, 2 MPa H_2, 5 kPa 1-butanol). Dashed lines represent trends.

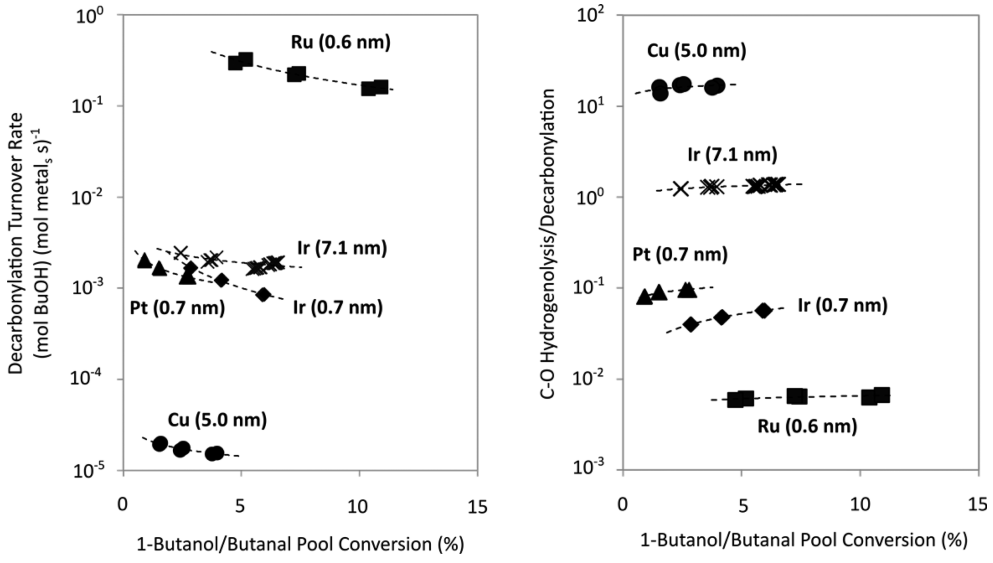

Figure 11. Effect of 1-butanol/butanal pool conversion on (a) decarbonylation turnover rates, and (b) C−O hydrogenolysis/decarbonylation rate ratio on 5 wt % Cu/SiO_2 (5.0 nm, ●), 1 wt % Ir/SiO_2 (0.7 nm, ◆), 3 wt % Ir/SiO_2 (7.1 nm, x), 0.5 wt % Ru/SiO_2 (0.6 nm, ■), (523 K, 2 MPa H_2, 5 kPa 1-butanol), and 1 wt % Pt/SiO_2 (0.7 nm, ▲), (498 K, 2 MPa H_2, 5 kPa 1-butanol). Dashed lines represent trends.

which is reflected by decreasing turnover rates with increasing CO pressure (with increasing 1-butanol/butanal pool conversion). Such inhibition is expected from large CO* binding energies on these metals (−166 kJ mol^{-1} on Ir(111), −129 kJ mol^{-1} on Pt(111), −162 kJ mol^{-1} on Ru(0001) calculated in this work for isolated CO*). Similar considerations lead us to conclude that strong CO inhibition effects will also prevail on Rh, Ni, and Pd catalysts (CO binding energies: −153 kJ mol^{-1} on Rh(111), −119 kJ mol^{-1} on Ni(111), and −104 kJ mol^{-1} on Pd(111), as calculated by DFT).

CO* species formed from decarbonylation can undergo secondary reactions with H_2 to form CH_4. The CH_4/C_3H_8 ratio in the products represents the fraction of CO* that undergoes secondary methanation reactions, which increases with increasing conversion (Figure 10b). CH_4/C_3H_8 ratios were much larger on Ru than on Ir or Pt (483 K, 5 kPa 1-butanol, 2 MPa H_2, Figure 10b); such higher CH_4 selectivities are consistent with methanation turnover rates that are ∼10-fold higher on Ru than on Pt and Ir clusters.[56] Surfaces that scavenge CO* via reactions with hydrogen to form CH_4 will decrease CO pressures and CO* coverages, thus decreasing CO-inhibition effects (Figure 10a). Methanation, as the CO scavenging route, however, gives rise to H_2 consumption stoichiometries

$$C_3H_7CH_2OH + 2H_2 \rightarrow CH_4 + C_3H_8 + H_2O \quad (9)$$

that are even higher than for C−O hydrogenolysis

$$C_3H_7CH_2OH + H_2 \rightarrow C_4H_{10} + H_2O \quad (10)$$

Thus, strategies that combine decarbonylation with methanation are more H_2-intensive than C−O hydrogenolysis, a reaction that altogether avoids CO formation and thus its strong inhibition effects.

DOI: 10.1021/jacs.5b05361
J. Am. Chem. Soc. 2015, 137, 11984−11995

Measured decarbonylation turnover rates on Cu/SiO_2 (5.0 nm) were >100 times lower than on Ir (0.7 or 7.1 nm) and Ru (0.6 nm) clusters at 523 K and Pt clusters (0.7 nm) at 483 K (Figure 11a). The lower decarbonylation turnover rates on Cu may reflect the required formation of two M−C bonds at the transition state (on Ir, Figure 8A) that mediate this reaction and the weak nature of such bonds at Cu surfaces; C* binding energies (BE_{C*}) are significantly lower on Cu(111) (−438 kJ mol^{-1}) than on Ru(0001) (−698 kJ mol^{-1}), Ir(111) (−688 kJ mol^{-1}) or Pt(111) (−685 kJ mol^{-1}). These low C−C hydrogenolysis rates also appear to reflect the much weaker binding of CO* on Cu (111) (−46 kJ mol^{-1}) than on Ru (0001), Ir (111), or Pt (111) (−162 kJ mol^{-1}, −166 kJ mol^{-1}, −129 kJ mol^{-1}, respectively). C−O hydrogenolysis rates, on the other hand, vary much less with changing metal composition than those of decarbonylation. The very low decarbonylation rates on Cu in turn lead to high C−O hydrogenolysis selectivities (ratios of C−O to C−C hydrogenolysis >15, Figure 11b). This correlation is plausible given that the C−C cleavage transition state (on Ir, Figure 8A) involves two C−M bonds, while the C−O cleavage transition state includes only one (on Ir, Figure 8B). These C−C cleavage transition states thus become much less stable than C−O cleavage transition states (which may have an additional M−O bond depending on the mechanism) on surfaces that bind C* weakly, as on Cu surfaces, in comparison to Ir, Pt, or Ru surfaces. This leads to lower concentrations of the C−C cleavage transition states compared to that of C−O cleavage and consequently to higher C−O hydrogenolysis selectivities on Cu.

Among the metals examined here, only Cu selectively catalyzes C−O hydrogenolysis. C−O hydrogenolysis preserves valuable C atoms in the products and avoids strong inhibition by CO*, making it the preferred route for deoxygenation of alkanol/alkanal mixtures. Other Group IX metals (Ag and Au) also bind C* weakly (BE_{C*}: −282 kJ mol^{-1} and −382 kJ mol^{-1} on Ag (111) and Au (111)) compared to Cu (111) (BE_{C*}: −438 kJ mol^{-1}) or Group VIII metals (Ru, Rh, Pd, Os, Ir, and Pt) (BE_{C*}: − 616 to −702 kJ mol^{-1}) and thus are expected to exhibit low C−C cleavage rates. Their significantly weaker M−C bonds on terrace sites are also expected to lead to low C−O hydrogenolysis turnover rates, however, requiring the presence of low-coordination surface atoms that prevail on small Ag and Au clusters to achieve high C−O hydrogenolysis selectivities.

4. CONCLUSIONS

Decarbonylation is the main decomposition pathway of 1-butanol on Group VIII metals, such as Ir, Pt, and Ru. The main product of decarbonylation, CO, is a strong inhibitor, resulting in decreasing turnover rates with alkanol/alkanal pool conversion. Analyses of decarbonylation turnover rates indicate that at the reaction conditions used in this study (1−5 kPa 1-butanol, 1−3 MPa H_2, and 1−10 kPa CO at 523 K), Ir clusters are covered with chemisorbed CO* species, and the kinetically relevant transition state has three fewer H atoms than 1-butanol. These kinetic data, combined with DFT calculations of reaction and activation enthalpies across a series of RCHO*, RCOH*, and RCO* intermediates (R = CH_3CH_2, CH_3CH, CH_3C), indicate that C−C cleavage proceeds in CH_3C*C*O intermediates following the kinetically relevant C−H activation of CH_3CH_2CO* to form CH_3CHCO*. C−C hydrogenolysis in 1-butanol/butanal occurs only at the C−C bond vicinal to the O atom because the C═O double bond in RCCO* significantly weakens the adjacent C−C bond. DFT calculations demonstrate that C−O hydrogenolysis proceeds through an H*-assisted C−O activation of the CH_3CH_2CHOH* intermediate, leading to rates proportional to alkanol pressure and independent of H_2 pressure, consistent with experimental measurements. C−O hydrogenolysis turnover rates become comparable to decarbonylation rates as the cluster size of Ir is increased from 0.7 to 7 nm because C−O hydrogenolysis preferentially takes place on high-coordination Ir sites due to strongly adsorbed CO* blocking corner/edge sites. The use of large metal clusters, however, is inefficient as the majority of the precious metal is inaccessible. CO inhibition can instead be alleviated by coupling decarbonylation with methanation on metals such as Ru. Methanation, however, has a higher H_2 requirement than C−O hydrogenolysis. Group VIII metals are not ideal deoxygenation catalysts if C−C activations and H_2 consumption need to be minimized. Cu, on the other hand, is unique in its ability to catalyze C−O hydrogenolysis selectively over C−C hydrogenolysis because of weak binding of C* and CO*. This is crucial for the conversion of many biomass-derived intermediates with alkanol/alkanal functionalities to chemicals and fuels.

■ ASSOCIATED CONTENT

Supporting Information

The Supporting Information is available free of charge on the ACS Publications website at DOI: 10.1021/jacs.5b05361.

Methodological details, figures containing DFT-derived structures for all calculations herein, and further discussions of ruled-out C−O hydrogenolysis mechanisms, particle size effects, and the low coverages of H* on Ir surfaces (PDF)

■ AUTHOR INFORMATION

Corresponding Author

*iglesia@berkeley.edu

Notes

The authors declare no competing financial interest.

■ ACKNOWLEDGMENTS

This material is based upon work supported by the U.S. Department of Energy, Office of Science, Office of Basic Energy Sciences, Chemical Sciences Division of the US Department of Energy as well as by XSEDE (CHE130022) and EMSL (Proposal 47800) for computational resources. The authors acknowledge Mr. Will Knaeble and Dr. Shuai Wang for helpful discussions.

■ REFERENCES

(1) Roman-Leshkov, Y.; Barrett, C. J.; Liu, Z. Y.; Dumesic, J. A. *Nature* **2007**, *447*, 982.

(2) Chheda, J. N.; Huber, G. W.; Dumesic, J. A. *Angew. Chem., Int. Ed.* **2007**, *46*, 7164.

(3) Davda, R. R.; Shabaker, J. W.; Huber, G. W.; Cortright, R. D.; Dumesic, J. A. *Appl. Catal., B* **2005**, *56*, 171.

(4) Braunchweig, B.; Hibbitts, D.; Neurock, M.; Wieckowski, A. *Catal. Today* **2013**, *202*, 197.

(5) Hibbitts, D. D.; Neurock, M. *J. Catal.* **2013**, *299*, 261.

(6) Davda, R. R.; Shabaker, J. W.; Huber, G. W.; Cortright, R. D.; Dumesic, J. A. *Appl. Catal., B* **2003**, *43*, 13.

(7) Boga, D. A.; Oord, R.; Beale, A. M.; Chung, Y.-M.; Bruijnincx, P. C. A.; Weckhuysen, B. M. *ChemCatChem* **2013**, *5*, 529.

DOI: 10.1021/jacs.5b05361
J. Am. Chem. Soc. 2015, 137, 11984−11995

(8) Kunkes, E. L.; Simonetti, D. A.; West, R. M.; Serrano-Ruiz, J. C.; Gärtner, C. A.; Dumesic, J. A. *Science* **2008**, *322*, 417.
(9) Davis, J. L.; Barteau, M. A. *J. Am. Chem. Soc.* **1989**, *111*, 1782.
(10) Davis, J. L.; Barteau, M. A. *Surf. Sci.* **1990**, *235*, 235.
(11) Davis, J. L.; Barteau, M. A. *Surf. Sci.* **1987**, *187*, 387.
(12) Gates, S. M.; Russell, J. N.; Yates, J. T. *Surf. Sci.* **1986**, *171*, 111.
(13) Sexton, B. A.; Rendulic, K. D.; Hughes, A. E. *Surf. Sci.* **1982**, *121*, 181.
(14) Ferrin, P.; Simonetti, D.; Kandoi, S.; Kunkes, E.; Dumesic, J. A.; Nørskov, J. K.; Mavrikakis, M. *J. Am. Chem. Soc.* **2009**, *131*, 5809.
(15) Mavrikakis, M.; Barteau, M. A. *J. Mol. Catal. A: Chem.* **1998**, *131*, 135.
(16) Gursahani, K. I.; Alcalá, R.; Cortright, R. D.; Dumesic, J. A. *Appl. Catal., A* **2001**, *222*, 369.
(17) Alcalá, R.; Mavrikakis, M.; Dumesic, J. A. *J. Catal.* **2003**, *218*, 178.
(18) Kandoi, S.; Greeley, J.; Simonetti, D.; Shabaker, J.; Dumesic, J. A.; Mavrikakis, M. *J. Phys. Chem. C* **2011**, *115*, 961.
(19) Liu, B.; Greeley, J. *J. Phys. Chem. C* **2011**, *115*, 19702.
(20) Flaherty, D. W.; Hibbitts, D. D.; Gürbüz, E. I.; Iglesia, E. *J. Catal.* **2014**, *311*, 350.
(21) Flaherty, D. W.; Iglesia, E. *J. Am. Chem. Soc.* **2013**, *135*, 18586.
(22) Sitthisa, S.; Resasco, D. *Catal. Lett.* **2011**, *141*, 784.
(23) Sitthisa, S.; Sooknoi, T.; Ma, Y.; Balbuena, P. B.; Resasco, D. E. *J. Catal.* **2011**, *277*, 1.
(24) Deutsch, K. L.; Shanks, B. H. *Appl. Catal., A* **2012**, *447*−*448*, 144.
(25) Deutsch, K. L.; Shanks, B. H. *Appl. Catal., A* **2014**, *470*, 390.
(26) Soled, S. L.; Malek, A.; Miseo, S.; Baumgartner, J.; Kliewer, C.; Afeworki, M.; Stevens, P. A. *Stud. Surf. Sci. Catal.* **2006**, *162*, 103.
(27) Miller, J. T.; Schreier, M.; Kropf, A. J.; Regalbuto, J. R. *J. Catal.* **2004**, *225*, 203.
(28) McVicker, G. B.; Baker, R. T. K.; Garten, R. L.; Kugler, E. L. *J. Catal.* **1980**, *65*, 207.
(29) Choi, M.; Wu, Z.; Iglesia, E. *J. Am. Chem. Soc.* **2010**, *132*, 9129.
(30) *Handbook of Heterogenous Catalysis*; Ertl, G., Knozinger, H., Schuth, F., Weitkamp, J., Eds.; John Wiley and Sons: New York, 2008.
(31) Kresse, G.; Furthmuller, J. *Comput. Mater. Sci.* **1996**, *6*, 15.
(32) Kresse, G.; Furthmuller, J. *Phys. Rev. B: Condens. Matter Mater. Phys.* **1996**, *54*, 11169.
(33) Kresse, G.; Hafner, J. *Phys. Rev. B: Condens. Matter Mater. Phys.* **1993**, *47*, 558.
(34) Kresse, G.; Hafner, J. *Phys. Rev. B: Condens. Matter Mater. Phys.* **1994**, *49*, 14251.
(35) Blochl, P. E. *Phys. Rev. B: Condens. Matter Mater. Phys.* **1994**, *50*, 17953.
(36) Kresse, G.; Joubert, D. *Phys. Rev. B: Condens. Matter Mater. Phys.* **1999**, *59*, 1758.
(37) Hammer, B.; Hansen, L.; Norskov, J. K. *Phys. Rev. B: Condens. Matter Mater. Phys.* **1999**, *59*, 7413.
(38) Perdew, J.; Burke, K.; Ernzerhof, M. *Phys. Rev. Lett.* **1996**, *77*, 3865.
(39) Zhang, Y.; Yang, W. *Phys. Rev. Lett.* **1998**, *80*, 890.
(40) Henkelman, G.; Jonsson, H. A. *J. Chem. Phys.* **2000**, *113*, 9978.
(41) Jonsson, H. A.; Mills, G.; Jacobsen, K. W. *Nudged Elastic Band Method for Finding Minimum Energy Paths of Transitions*; World Scientific: Hackensack, NJ, 1998.
(42) Henkelman, G.; Jonsson, H. A. *J. Chem. Phys.* **1999**, *111*, 7010.
(43) Mavrikakis, M.; Barteau, M. A. *J. Mol. Catal. A: Chem.* **1998**, *131*, 135.
(44) Huber, G. W.; Shabaker, J. W.; Dumesic, J. A. *Science* **2003**, *300*, 2075.
(45) Goel, S.; Zones, S. I.; Iglesia, E. *J. Am. Chem. Soc.* **2014**, *136*, 15280.
(46) Lee, K.; Morikawa, Y.; Langreth, D. C. *Phys. Rev. B: Condens. Matter Mater. Phys.* **2010**, *82*, 155461.
(47) Maire, G.; Plouidy, G.; Prudhomme, J. C.; Gault, F. G. *J. Catal.* **1965**, *4*, 556.
(48) Cimino, A.; Boudart, M.; Taylor, H. *J. Phys. Chem.* **1954**, *58*, 796.
(49) Sinfelt, J. H.; Taylor, W. F.; Yates, D. J. C. *J. Phys. Chem.* **1965**, *69*, 95.
(50) Flaherty, D.; Uzun, A.; Iglesia, E. *J. Phys. Chem. C* **2015**, *119*, 2597.
(51) Tan, Q.; Hibbitts, D.; Neurock, M.*Unpublished results*, 2014
(52) Van Hardeveld, R.; Hartog, F. *Surf. Sci.* **1969**, *15*, 189.
(53) Allian, A.; Takanabe, K.; Fujdala, K.; Hao, X.; Truex, T.; Cai, J.; Buda, C.; Neurock, M.; Iglesia, E. *J. Am. Chem. Soc.* **2011**, *133*, 4498.
(54) Shustorovich, E. *Adv. Catal.* **1990**, *37*, 101.
(55) Loveless, B. T.; Buda, C.; Neurock, M.; Iglesia, E. *J. Am. Chem. Soc.* **2013**, *135*, 6107.
(56) Vannice, M. A. *J. Catal.* **1975**, *37*, 449.

DOI: 10.1021/jacs.5b05361
J. Am. Chem. Soc. 2015, 137, 11984−11995